International Journal of Multiphase Flow 77 (2015) 196–208

Contents lists available at ScienceDirect

International Journal of Multiphase Flow

journal homepage: www.elsevier.com/locate/ijmultiphaseflow

Numerical study of a flapping liquid sheet sheared by a high-speed stream

Nicolas Odier[a], Guillaume Balarac[a,*], Christophe Corre[b], Vincent Moureau[c]

[a] Grenoble-INP / CNRS / UJF-Grenoble 1, LEGI UMR 5519, Grenoble F-38041, France
[b] Ecole Centrale de Lyon, LMFA UMR 5509, Ecully F-69134, France
[c] Normandie Université / CNRS / INSA de Rouen, CORIA UMR 6614, St Etienne du Rouvray F-76801, France

ARTICLE INFO

Article history:
Received 1 April 2015
Revised 27 June 2015
Accepted 2 August 2015
Available online 3 September 2015

Keywords:
Two-phase flow
Flapping liquid sheet
Vortical structures
Sensibility study
Boundary-layer thickness

ABSTRACT

A numerical study of a liquid sheet sheared on both sides by a high-speed stream is performed in this work, at moderate density and velocity ratio between phases. Near the injection, an interfacial wave develops on both interfaces of the liquid sheet. A vortical detachment of the high-speed stream is observed behind this wave and modifies the pressure field around the sheet. The global flapping mechanism is a consequence of the pressure difference between the two sides of the liquid sheet. The flapping dynamics is characterized and compared to existing correlations available in the literature. A sensitivity study of the flapping dynamics to the high-speed stream boundary layer thickness is performed and a relevant Strouhal number is proposed.

Introduction

Air-assisted liquid jets are widely studied because of their key use in aircraft propulsion systems, where a fuel is mixed with a comburant through an atomization process. In most aeronautical engines, an annular jet of a liquid fuel is sheared on both sides by a fast gas. In rocket engines, an axial jet of liquid comburant is sheared by a high-speed gaseous oxidizer. For both geometries, the liquid jet can be subject to a flapping motion under some specific conditions (Leboucher et al., 2009; Matas and Cartelier, 2013) and the flapping occurrence influences the size of produced droplets. Understanding the conditions of flapping occurrence and characterizing this flapping motion is therefore of interest to improve the combustion efficiency. A geometrically simplified configuration has been the subject of thorough investigation over the past years: the planar liquid sheet, where a planar liquid (often water, or kerosene) sheet is sheared on both sides by fast gas (air), has been widely studied by Mansour and Chigier (1991), Carentz (2000), Carvalho et al. (2002), Lozano and Barreras (2001a; 2001b), Lozano et al. (2005). Even though it is still unclear whether the flapping dynamics of a planar liquid sheet on one hand and of a coaxial jet on the other hand are comparable, previous works devoted to coaxial flapping (Matas and Cartelier, 2013) made an attempt at drawing some parallel between the phenomena observed on both configurations. Despite the geometrical simplification with respect to industrial configurations, the basic phenomena leading to the flapping motion on the academic plane configuration still remain poorly understood, especially because of the large number of parameters involved in the flapping process. Furthermore, the experimental investigation of the interaction between gaseous vortices and the liquid jet – suspected to be a main cause of this flapping motion (Lozano and Barreras, 2001a; Matas et al., 2011) – remains hard to tackle experimentally.

Note that while the dynamics of the liquid sheet, a system of two interfaces, remains poorly understood, the destabilizing mechanisms occuring in the case of a single liquid interface sheared by a fast gas is better known. Marmottant (Marmottant and Villermaux, 2004) and Ben Rayana (Ben Rayana, 2007) describe a mechanism where the development of a primary instability leads to an interfacial wave. A secondary instability leads to a ligamental development on this interfacial wave, with these ligaments breaking into droplets. To predict the occurrence frequency of the first instability, the gaseous vorticity thickness δ_g in the gas has been identified by theoretical analysis as a crucial parameter. Matas et al. (2011) predicted that the wavenumber k evolves as $k = (\sqrt{2} + \frac{3}{2}M^{-\frac{1}{2}})\frac{\sqrt{r}}{\delta_g}$ and the pulsation ω as $\omega = r\frac{U_g}{\delta_g}(1 + \frac{5}{2}\sqrt{2}M^{-\frac{1}{2}})$, with $r = \frac{\rho_g}{\rho_l}$ the gas to liquid density ratio and $M = \frac{\rho_g U_g^2}{\rho_l U_l^2}$ the gas to liquid momentum flux ratio. More recently, Fuster et al. (2013) showed that a transition from a

* Corresponding author. Tel.: +33476825142.
E-mail addresses: nicolas.odier@legi.grenoble-inp.fr (N. Odier), guillaume.balarac@legi.grenoble-inp.fr (G. Balarac), christophe.corre@ec-lyon.fr (C. Corre), vincent.moureau@coria.fr (V. Moureau).

http://dx.doi.org/10.1016/j.ijmultiphaseflow.2015.08.001
0301-9322/

convective to absolute instability can occur if this gaseous vorticity thickness δ_g reaches some critical conditions. The experimental measurement of this quantity remains unfortunately hard to perform accurately, because δ_g is usually very thin (typically 300 μ_m) and difficult to prescribed experimentally.

Based on the current knowledge, the study of a liquid sheet sheared on both sides by a fast gas involves the analysis of the interactions between the vortical structures in the gas and the gas/liquid interface, with a particular attention paid to the control of the gaseous boundary layer. The present work proposes to perform such a study by taking advantage of the high predictive capacity achieved by state-of-the-art direct numerical simulation solvers.

Numerical simulation for atomization remains very challenging because of the density jump that must be discretized through the interface, the strong velocity gradients and the multiple topology changes taking place in the flow. In the past decade, various strategies have however enabled the direct numerical simulation of a liquid jet development in a gas with higher and higher density and velocity ratio. Menard et al. (2007) coupled the Level-Set method and the Volume of Fluid (VOF) method to simulate a diesel jet with a density ratio of 27. This coupling (CLSVOF) has been later used by Shinjo and Umemura (2010; 2011) to study the spray formation of a diesel jet, on a mesh refined up to 6 billions grid points. Desjardins et al. (2008) computed a similar jet with a density ratio of 40, using an accurate conservative Level-Set method (ACLS). More recently, Desjardins et al. (2013) achieved some computations of an experiment in dodecane/nitrogen conditions inspired from Marmottant's work. Other strategies, such as adaptative mesh refinement (AMR), have been used for instance by Fuster et al. (2009) to compute a 2D simulation of Ben-Rayana's experiment (Ben Rayana, 2007) and of Marmottant's experiment (Marmottant, 2001) at moderate density ratio, or by Berlemont et al. (2012) to compute Ben Rayana's experiment in actual air/water conditions. Herrmann (2008) proposed a Refined Level-Set grid method (RGLS) to track the interface on a grid distinct from the one used to solve the Navier–Stokes equations and later proposed (Herrmann, 2010) to couple this method with a Lagrangian description of the flow to track the drops created by the atomization process. The RGLS method has also been used by Kim and Moin (2011) to compute Marmottant's experiment, with actual density and velocities of air and water.

Increasing density and velocity ratios to reach values close or equal to those encountered in experiments requires smaller and smaller mesh sizes which induces in turn an increasingly high computational cost. This cost tends to limit the knowledge gained from a direct numerical simulation giving access to detailed flow features, because the simulation is usually limited to a single configuration. Consequently, the methodology proposed in the present study differs from the one followed in the above cited works. To perform a thorough physical investigation of the flapping mechanism, the direct numerical simulation of a liquid sheet sheared by a high-speed stream is performed for moderate density ratio, with in particular a variation of some influential parameters requiring a whole series of computations, allowed by the not too excessive computational cost associated with the retained moderate density ratio. Taking full advantage of the complete set of local flow properties provided by direct numerical simulations, the present work provides a detailed physical scenario for the flapping dynamics, a quantitative characterization of the flapping phenomenon including comparison with previous studies of the literature and a sensitivity study of flapping to the high-speed stream boundary-layer thickness.

The paper is organized as follows: the flow configuration is described in section “Flow configurations and numerical parameters” where the main parameters involved in the computational flow analysis are also reviewed. Section “Flapping dynamics: mechanism and characterization” investigates the physical mechanism leading to the flapping; the quantitative characteristics of the flapping phenomenon is also analyzed and compared to previous studies of the literature. A detailed sensitivity study of flapping to the high-speed stream boundary-layer thickness is presented in section “Influence of the high-speed stream initial boundary layer thickness”. Conclusions are drawn and work perspectives are proposed in section “Conclusion”.

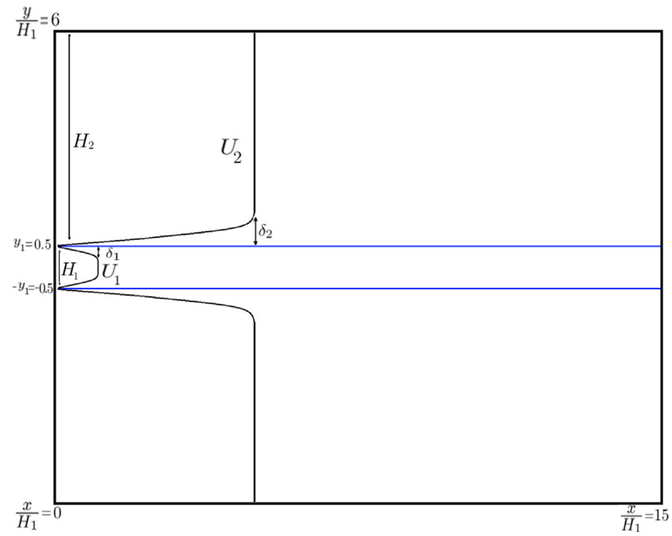

Fig. 1. Schematic view of the inlet conditions for the configuration under study.

Flow configurations and numerical parameters

The numerical solver used in this work to compute the flow of interest is YALES2, developed at CORIA, France. This is a massively parallel unstructured code, solving the Navier–Stokes equations with a finite-volume formulation with numerical schemes of 4th order in time and space. More details on the schemes can be found in Enjalbert (2006); Vantieghem (2011); Malandain (2013). The interface tracking is ensured by using an accurate conservative Level-Set method (Desjardins et al., 2008), coupled with the ghost-fluid method (Desjardins and Moureau, 2010). From the numerical point of view, the main computational challenge on massively parallel machines lies in the solving of the Poisson equation, in which the problem matrix features variable coefficients and the solution (the dynamic pressure) is discontinuous at the gas/liquid interface. These two particularities strongly limit the choice of the linear solver and dedicated two-level solvers have been developed (Malandain et al., 2013). The whole methodology has been validated on numerous canonical test cases and the demonstration of its applicability to realistic two-phase flows was performed for the so-called Triple Disk Injector from Grout et al. (2007) as shown in Malandain et al. (2013).

The flow configuration studied in this work is a plane jet surrounded by another faster phase, as illustrated in Fig. 1. The dimension of the computational box is $15H_1 \times 12H_1 \times 4H_1$ (respectively length, height and width of the domain), where H_1 is the liquid sheet thickness. U_1 and U_2 are respectively the inner liquid jet and the high-speed stream velocity, and δ_1 and δ_2 are the boundary layer thicknesses for the inner liquid jet and for the high-speed stream, respectively. In this work, velocities are normalized by the high-speed stream velocity U_2, and lengths by the liquid jet thickness H_1.

A Polhausen-type polynomial is used to describe the symmetric inlet velocity profile (Couderc, 2007). The upper part of this profile is

Table 1
Physical parameters of each phase.

Phase	ρ_i	μ_i	U_i	δ_i	σ
Liquid ($i = 1$)	10.0	5.0e−4	0.1666	0.1	0.002
High-speed stream ($i = 2$)	1.0	2.5e−4	1.0	0.1	

Table 2
Nomenclature.

Symbol	Signification
$_1$	Relative to the liquid phase
$_2$	Relative to the high-speed stream phase
H_1	Initial liquid sheet thickness
ρ_i	Density
μ_i	Dynamic viscosity
U_i	Velocity
δ_i	Boundary layer thickness
σ	Surface tension

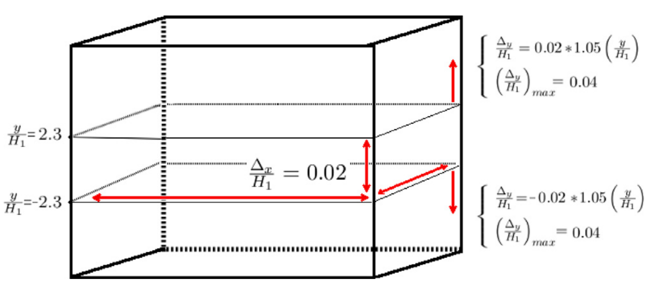

Fig. 2. Mesh size distribution in the computational box.

then defined as:

$$U(y) = \begin{cases} U_2 & \text{for } y > H_1 + \delta_2 \\ U_2\left(2\eta - 2\eta^3 + \eta^4\right) \text{ with } \eta = \frac{y-H_1}{\delta_2} & \text{for } H_1 < y < H_1 + \delta_2 \\ U_1\left(-2\eta + 2\eta^3 + \eta^4\right) \text{ with } \eta = \frac{y-H_1}{\delta_1} & \text{for } H_1 - \delta_1 < y < H_1 \\ U_1 & \text{for } 0 < y < H_1 - \delta_1, \end{cases} \tag{1}$$

Note that the velocities in the normal y, and spanwise z directions are set to zero plus a random noise of 5% of U_2 at the inlet. Periodic conditions are imposed on laterals boundaries, and a sponge layer is included upstream of the outlet condition.

The Reynolds number based on the outer stream fluid properties and on the jet thickness, is $Re = \frac{\rho_2 U_2 H_1}{\mu_2} = 4000$, with ρ_2 and μ_2, the density and the dynamic viscosity of the outer fluid. The Weber number based on the outer stream fluid properties and on the jet thickness, is $We = \frac{\rho_2 U_2^2 H_1}{\sigma} = 500$, with σ the surface tension. Finally, the density ratio is $r_\rho = \rho_1/\rho_2 = 10$ and the dynamic viscosity ratio is $\mu_1/\mu_2 = 2$. All physical parameters are summarized in Tables 1, and 2 that define those parameters.

The mesh size Δ_x is chosen such that the smallest boundary layer thickness ($\frac{\delta_2}{H_1} = 0.1$) is described by five cells. The mesh size distribution in the x and y direction is summarized in Fig. 2; overall, the mesh contains 56 million cells.

Preliminary validation. Previous studies on the flapping dynamics (Mansour and Chigier, 1991; Lozano and Barreras, 2001b; Couderc, 2007) have established the flapping frequency which increases linearly with the outer velocity U_2. Reproducing this linear increase has been set as a preliminary accuracy requirement for the computations. A mesh convergence study has led to retain the above described mesh refinement, which yields the expected linear increase of the flapping frequency with U_2 as displayed in Fig. 3. All the results analyzed in the following sections have been obtained using this fine mesh.

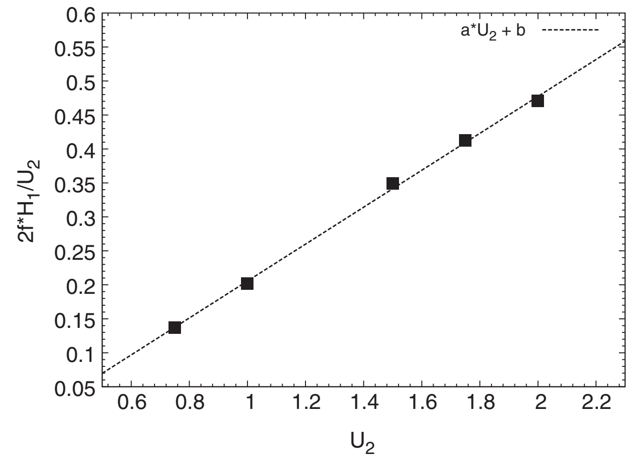

Fig. 3. Linear evolution of the flapping frequency with U_2.

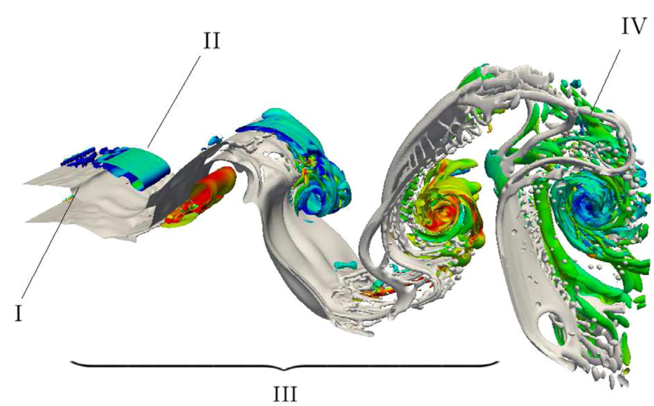

Fig. 4. Global flow picture: contour of interface (grey) and contours of Q-Criterion $Q = 0.3\left(\frac{U_2}{H_1}\right)^2$ colored by spanwise vorticity (blue stands for negative values of vorticity, yellow for positive values). (For interpretation of the references to color in this figure legend, the reader is referred to the web version of this article.)

Flapping dynamics: mechanism and characterization

Global flow picture

The instantaneous flow dynamics at the non-dimensional time $t = 141$ (normalized by $(\frac{H_1}{U_2})$) is captured in Fig. 4, where the instantaneous contours of the interface between the liquid and the high-speed stream are plotted in grey along with the contour of the Q criterion, corresponding to the non-dimensional value $Q = 0.3$ (normalized by $(\frac{U_2}{H_1})^2$), colored by the spanwise vorticity. The Q criterion, has been proposed in Hunt et al. (1988), as $Q = \frac{1}{2}(\Omega_{ij}\Omega_{ij} - S_{ij}S_{ij})$, where $\Omega_{ij} = \frac{1}{2}(\frac{\partial u_i}{\partial x_j} - \frac{\partial u_j}{\partial x_i})$ and $S_{ij} = \frac{1}{2}(\frac{\partial u_i}{\partial x_j} + \frac{\partial u_j}{\partial x_i})$ to identify coherent structures in a flow, and the value 0.3 is well adapted for the flow under study. Deep to light blue stands for negative value of vorticity while yellow to red corresponds to positive values.

The global oscillation of the plane liquid jet takes place over an extended region in the y direction. A close look at the interface near the inlet section allows to observe transverse deformations on both sides of the liquid sheet (item *I* in Fig. 4). Behind those waves, the detachment of vortical structures is observed in the high-speed stream (item *II* in Fig. 4). Such a vortical detachment behind a liquid obstacle has been experimentally evidenced in Lozano and Barreras (2001a) on a planar liquid sheet, and in Matas et al. (2011)

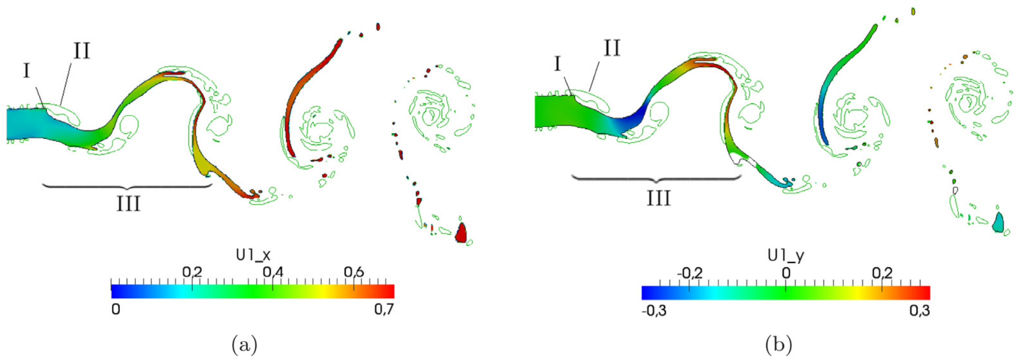

Fig. 5. Transverse 0xy plane colored by the x component (left) and the y component (right) of the liquid velocity U_1. Contours of interface (black) and of Q criterion $Q = 0.3\left(\frac{U_2}{H_1}\right)^2$ (green). (For interpretation of the references to color in this figure legend, the reader is referred to the web version of this article.)

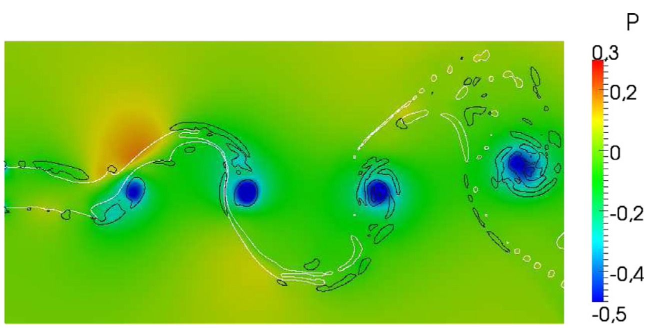

Fig. 6. Transverse plane colored by $\frac{P-P_{ref}}{\rho}$. Instantaneous contour of interface (white) and contours of Q criterion $Q = 0.3\left(\frac{U_2}{H_1}\right)^2$ (black).

on a coaxial jet. Another noticeable aspect is the thinning of the liquid sheet (item *III* in Fig. 4) and its breakup into ligaments (item *IV* in Fig. 4), described in Stapper and Samuelsen (1990) as a “stretched streamwise ligament” mode.

Fig. 5 displays a transverse *Oxy* plane of the flow, where the liquid is successively colored by the streamwise and transverse components of the liquid velocity. The contour 0.3 of the normalized Q criterion is also reported. The liquid acceleration induced by the shear imposed by the high-speed stream can be clearly observed on this plot. This acceleration is responsible for the sheet thinning, to ensure liquid flowrate conservation as explained in Couderc (2007). The detachment of vortical structures (identified by the Q criterion) in the fastest phase, behind interfacial waves, is also clearly visible in Fig. 5.

As can be observed in Fig. 6, displaying the pressure field in this same transverse *Oxy* plane, the detached vortical structures induce a decrease of pressure behind their corresponding side of the sheet. The opposite side of the sheet is an obstacle for the high-speed stream, which reduces its velocity and yields an increase in the pressure field. The coupling between these low and high pressure area is responsible for the flapping dynamics.

This mechanism occurs between the injection boundary and the first maximum of flapping amplitude. The flapping sheet can be seen as a “screen”, protecting the rest of the liquid from the interaction of the high-speed stream. The coupling between the high and low pressure area is observable at this first maximum flapping amplitude. For the other maximum flapping amplitude, only a low pressure area induced by recirculating structures is distinguished and the liquid sheet is only subject to this vortical advection.

Flapping characterization through average quantities

The above description of the physical mechanism leading to flapping remains qualitative; the remainder of Section “Flapping dynamics: mechanism and characterization” is devoted to a quantitative characterization of the flapping phenomenon, through a careful analysis of computed average quantities.

Definitions

The liquid characteristic function χ is defined at any time t as

$$\chi(\mathbf{x}, t) = \begin{cases} 1 & \text{if } \mathbf{x} \text{ is in liquid} \\ 0 & \text{otherwise} \end{cases} \tag{2}$$

with $\mathbf{x}$ the position vector. The liquid velocity is then defined as $U_1(\mathbf{x}, t) = \chi(\mathbf{x}, t) \cdot U(\mathbf{x}, t)$ with $U(\mathbf{x}, t)$ the flow speed while the high speed stream velocity is defined as $U_2(\mathbf{x}, t) = (1 - \chi(\mathbf{x}, t)) \cdot U(\mathbf{x}, t)$.

The time-average of a function $f(\mathbf{x}, t)$ is computed as:

$$\langle f(\mathbf{x}, t)\rangle = \frac{1}{(T_2 - T_1)} \int_{T_1}^{T_2} f(\mathbf{x}, t)\, dt, \tag{3}$$

The average liquid rate is then defined as $\alpha(\mathbf{x}) = \langle \chi(\mathbf{x}, t)\rangle$. Average liquid velocities and high-speed stream velocities are similarly and respectively defined as :

$$\langle U(\mathbf{x})\rangle_1 = \left\langle \left(\frac{\chi(\mathbf{x}, t) \cdot U(\mathbf{x}, t)}{\chi(\mathbf{x}, t)} \right) \right\rangle,$$

$$\langle U(\mathbf{x})\rangle_2 = \left\langle \left(\frac{(1 - \chi(\mathbf{x}, t)) \cdot U(\mathbf{x}, t)}{1 - \chi(\mathbf{x}, t)} \right) \right\rangle$$

T_1 and T_2 are chosen so that the flow dynamics displays at least 10 flapping periods.

Core length – flapping distance

The evolution of average quantities with the downstream distance x is displayed in Fig. 7(a). The widening of the area reached by the liquid because of the flapping dynamics can be clearly observed, as well as the merging process of the two velocity profiles, leading to a more homogeneous velocity distribution. Both velocity profiles indeed reach an average value close to $\frac{\langle U\rangle_i}{U_2} \simeq 0.7$.

The liquid core L_{core} of the jet is defined as the distance along the x-axis, computed from the injection plane, where the liquid rate becomes lower than 0.9. Since the liquid rate is decreasing with the axial distance x, the quantity L_{core} is computed as:

$$\alpha(L_{core}, 0, 0) = \langle \chi(L_{core}, 0, 0)\rangle = 0.9 \tag{4}$$

The threshold value 0.9 retained in (4) to defined L_{core} is partly arbitrary: a slightly lower or larger value could also be used. For all the computations presented in this work, a maximum dispersion of only $0.049H_1$ on the liquid core length evaluation has been observed when varying the value used in the criterion (4) from 0.85 to 0.95. This justifies the proposed value of 0.9 for the definition of L_{core} used in (4). The liquid core can be clearly identified on the left Fig. 7(b) where the contours of the average liquid rate are plotted in the *Oxy*

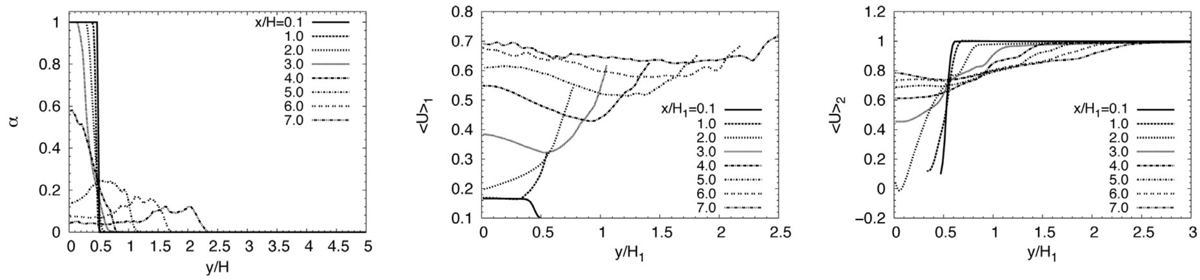

(a) Transversal profiles (along y) of average liquid rate (left), liquid velocity (center), and high-speed stream velocity (right) for selected x stations.

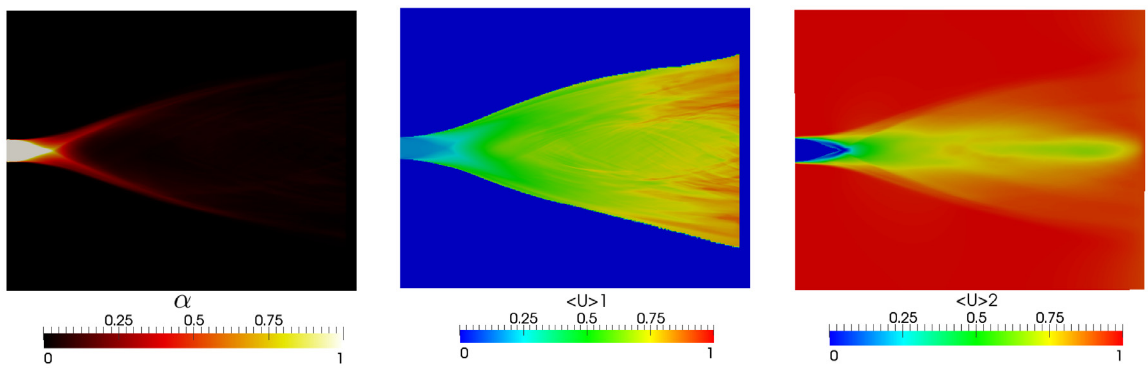

(b) Transverse Oxy plane colored by the average liquid rate (left), the liquid velocity (center), and the high-speed stream velocity (right).

Fig. 7. Average transversal profiles in the axial direction and transverse *Oxy* plane colored by average quantities.

plane, with the white-colored contours corresponding to values of α between 1 and 0.9. The core length is measured as:

$$\frac{L_{core}}{H_1} = 1.97 \simeq 2.0 \tag{5}$$

The flapping distance L_{flapp} is defined as the distance along the x-axis, computed from the injection, where the liquid rate becomes lower than 0.1:

$$\alpha(L_{flapp}, 0, 0) = \langle \chi(L_{flapp}, 0, 0) \rangle = 0.1 \tag{6}$$

The flapping distance can also be clearly identified on the left Fig. 7(b) where the contours of the average liquid rate are plotted in the *Oxy* plane, with the black-colored contours corresponding to values of α below 0.1. The flapping length is measured as:

$$\frac{L_{flapp}}{H_1} = 3.3 \tag{7}$$

To the authors' knowledge, there is no available experimental measurement of the liquid core L_{core} of a flapping liquid sheet. The measurable quantity is rather the break-up length. Some correlations however exist for the liquid core resulting from the atomization process where this liquid core is the remaining liquid part non-stripped by the high-speed stream (Eroglu et al., 1991; Woodwart, 1993; Engelbert et al., 1995; Lasheras et al., 1998; Raynal, 1997; Porcheron et al., 2002; Leroux et al., 2000). Since the liquid core studied in the present configuration is a consequence of a flapping behavior and not an atomization process, no agreement with previous authors has been found as it can be shown is Table 3. Matas and Cartelier (2013) have also pointed out the difficulty of comparing their liquid core measurement of a coaxial jet displaying both a flapping dynamics and an atomization process, with the established correlation in Lasheras et al. (1998) for a liquid core resulting for the atomization process. Table 3 also evidences significant discrepancies between the liquid core lengths predicted using a range of available correlations. These correlations rely on various combinations of non-dimensional numbers, such as a characteristic Reynolds number, a Weber number, an Ohnesorge number, the density ratio and the momentum flux ratio to express a law of variation for the non-dimensional liquid core length. Each of these correlations has usually been independently assessed by a research team using a specific experimental setup with an associated range of variation for the dimensional physical parameters which eventually leads to a range of variation for the non-dimensional numbers which seldom overlap from one experiment to the other. The observed discrepancies can thus be interpreted as the sign the validity of the proposed correlations is actually limited to a specific range of values for the non-dimensional numbers.

Spatial amplification growth rate

The spatial amplification growth rate k^* is defined from the evolution of the average liquid rate in the *Oxy* plane, $\alpha(x, y, 0) = \langle \chi(x, y, 0, t) \rangle$. The shape functions describing the envelope of the flapping liquid sheet are computed from:

$$\phi_1(x^*) \text{ as } \alpha(x^*, \phi_1(x^*)) = 0.05 \text{ and } \phi_1(x^*) > 0, \tag{8}$$

$$\phi_2(x^*) \text{ as } \alpha(x^*, \phi_2(x^*)) = 0.05 \text{ and } \phi_2(x^*) < 0, \tag{9}$$

with x^* the non-dimensional abscissa $x^* = x/H_1$. The spatial amplification growth rate k^* is then defined by fitting the average flapping shape $\phi(x^*)$:

$$\phi(x^*) = \frac{\phi_1(x^*) + \phi_2(x^*)}{2}, \tag{10}$$

with an exponential evolution of the form:

$$\phi(x^*) = \eta_0 e^{k^* \cdot x^*} \tag{11}$$

From the evolution of $\phi(x^*)$ displayed in Fig. 8, it can be noticed this exponential fit is actually valid from small values of x^* close to the injection plane until an inflexion point, reached for $x^* \approx 4$.

Table 3
Confrontation of our measured liquid core length L_{core} with existing propositions for liquid core resulting from the atomization process. Non-dimensional numbers are defined in Table 4.

Authors	Geometry	Proposed correlation	Result with author's proposition	Present study result
Eroglu et al. (1991)	Coaxial	$\frac{L_{core}}{D_1} = 0.5\left(\frac{We_r}{2}\right)^{-0.4} Re_1^{0.6}$	$\frac{L_{core}}{H_1} = 10.9$	$\frac{L_{core}}{H_1} = 2.0$
Woodwart (1993)	Coaxial	$\frac{L_{core}}{D_1} = 9.5.10^{-3}\,\frac{\rho_2}{\rho_1}^{-\frac{0.36}{H}} We^{-\frac{0.22}{H}} Re_1^{0.68}$	$\frac{L_{core}}{H_1} = 1.49$	$\frac{L_{core}}{H_1} = 2.0$
Engelbert et al. (1995)	Coaxial	$\frac{2L_{core}}{D_2-D_1} = 10.6MR^{-0.3}$	$\frac{2L_{core}}{H_2-H_1} = 0.09$	$\frac{2L_{core}}{H_2-H_1} = 0.88$
Lasheras et al. (1998)	Coaxial	$\frac{L_{core}}{D_1} = \frac{6}{\sqrt{M}}$	$\frac{L_{core}}{H_1} = 3.16$	$\frac{L_{core}}{H_1} = 2.0$
Raynal (1997)	Liquid film on plane plate	$\frac{L_{core}}{2H_1} = \frac{6}{\sqrt{M}}$	$\frac{L_{core}}{2H_1} = 3.16$	$\frac{L_{core}}{2H_1} = 1.0$
Porcheron et al. (2002)	Coaxial	$\frac{L_{core}}{D_1} = 2.85\left(\frac{\rho_2}{\rho_1}\right)^{-0.38} Oh^{0.34} M^{-0.13}$	$\frac{L_{core}}{H_1} = 0.85$	$\frac{L_{core}}{H_1} = 2.0$
Leroux et al. (2000)	Coaxial	$\frac{L_{core}}{D_1} = 10M^{-0.3}$	$\frac{L_{core}}{H_1} = 0.34$	$\frac{L_{core}}{H_1} = 2.0$

Table 4
Definition of the non-dimensional numbers involved in Table 3.

Authors	Definition
Eroglu et al. (1991)	$Re_1 = \frac{\rho_1 U_1 D_1}{\mu_1}$, $We_r = \frac{\rho_2 (U_2-U_1)^2 D_1}{2\sigma}$
Woodwart (1993)	$We_r = \frac{\rho_2 (U_2-U_1)^2 D_1}{\sigma}$
Engelbert et al. (1995)	$MR = \frac{\rho_2 U_2^2 (D_2^2-D_1^2)^2}{\rho_1 U_1^1 D_1^2}$
Lasheras et al. (1998)	$M = \frac{\rho_2 U_2^2}{\rho_1 U_1^2}$
Porcheron et al. (2002)	$Oh = \frac{\mu_1}{\sqrt{\rho_1 D_1 \sigma}}$
Leroux et al. (2000)	$M = \frac{\rho_2 U_2^2}{\rho_1 U_1^2}$

Table 6
Comparison of the primary interfacial instability frequency between the present study and theoretical prediction.

Author	Proposition	Result with author's proposal	Present study result
Marmottant and Villermaux (2004)	$f = \frac{1.5}{2\pi}\sqrt{\frac{\rho_2}{\rho_1}}\frac{U_c}{\delta_\omega}$	$f = 0.87\left(\frac{U_2}{H_1}\right)$	$f = 0.113\left(\frac{U_2}{H_1}\right)$

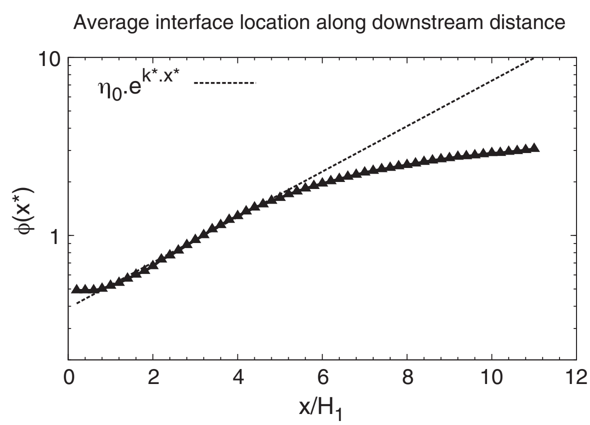

Fig. 8. Function $\phi(x^*)$ characterizing the average interface location. Fitting with exponential function: $f(x^*) = 0.4 \cdot e^{0.29 \cdot x^*}$.

Previous authors such as Carentz (2000), Lozano and Barreras (2001b) and Park et al. (2004) have experimentally studied this spatial amplification growth rate. A comparison between their experimental range of amplification growth rate, for the numerous experiments they performed, and the present numerical simulation is proposed in Table 5. No clear agreement between experimental measurements and our simulation can be found, (excepted the exponential shape of the envelope). The liquid sheet thickness may not be the right characteristic length to normalize the spatial amplification growth rate, but it is also likely the density ratio has a significant influence on the value of this spatial amplification growth rate, which would prevent a meaningful comparison.

Frequential characterization

Primary interfacial instability frequency

As pointed out in the opening description of the physical mechanism leading to flapping, a primary interfacial instability exists on both interfaces of the liquid sheet, and leads to the development of an interfacial waves (see Fig. 4).

The frequency of these waves is measured thanks to a set of probes located at $y/H_1 = 0.5$ in the *Oxy* plane and regularly spread in the *x*-direction on 500 equally spaced measurement points. The position $y^* = y/H_1 = 0.5$ corresponds to the initial position of the liquid sheet upper interface. Every probe located at $x/H_1 = x_k^*$ register the time evolution of the binary function $\chi(x_k^*, 0.5, 0, t)$. A Fast Fourier Transform is then applied to this temporal signal and the frequency obtained is associated to the primary interfacial instability frequency. The same process is performed on the temporal signal of the Q criterion, using the same set of probes, and the frequency obtained is associated to the frequency of vortical detachment behind the interfacial instability. The spectra obtained for $\chi(t)$ and $Q(t)$ are displayed in Fig. 9, colored by the FFT energetic component. The fundamental frequencies for both signals are found equal and given by:

$$f_{1st} = 0.113\left(\frac{U_2}{H_1}\right) \tag{12}$$

A comparison between the above frequency and the values proposed by previous authors using empirical correlations derived from linear stability analysis is proposed in Table 6. The frequency evolution of the primary instability is still subject to active research. Marmottant and Villermaux (2004), following Raynal's work (Raynal, 1997), has proposed an evolution law, based on a linear stability

Table 5
Comparison between the non-dimensional spatial amplification growth rate of the present study and experimental non-dimensional amplification growth rate reported in the literature.

References	Range of experimental k (mm^{-1})	Sheet thickness (mm)	Non-dimensional experimental k^*	Non-dimensional k^* of present study
Carentz (2000)	0.2–0.9	0.3	0.06–0.27	0.29
Lozano and Barreras (2001b)	0.1–0.45	0.35	0.035–0.158	0.29
Park et al. (2004)	0.1–0.35	0.254	0.0254–0.088	0.29

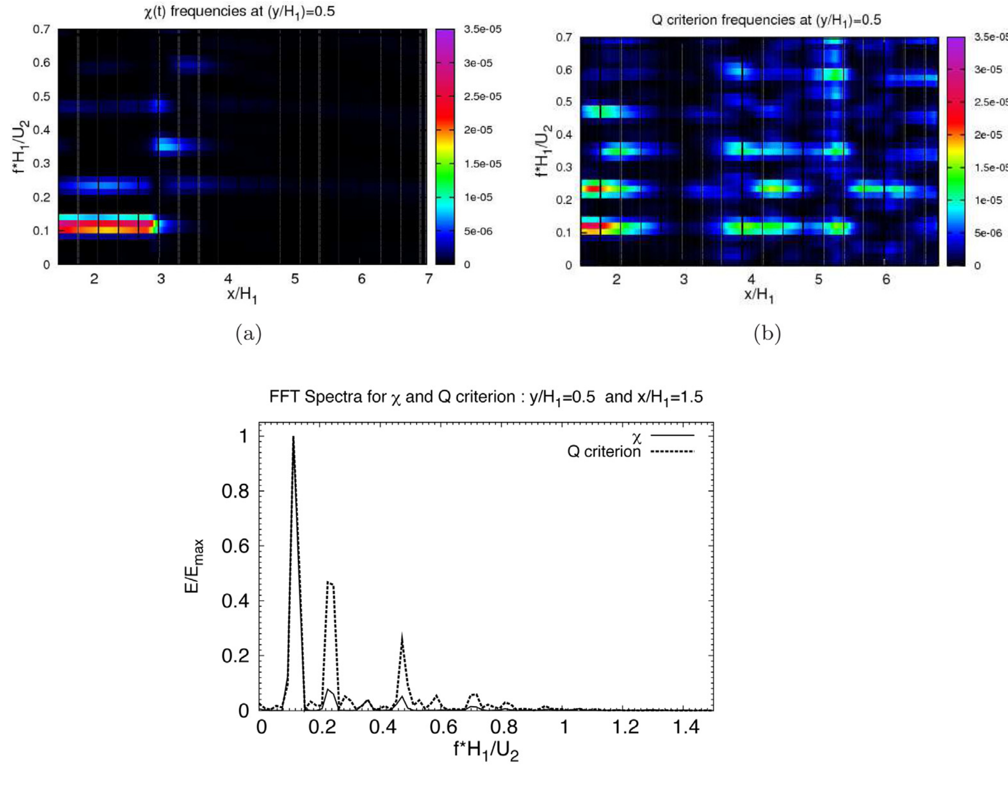

Fig. 9. (a and b) Comparison of the frequencies obtained on the temporal signals $\chi(t)$ and $Q(t)$ at $\frac{y}{H_1} = 0.5$, for $\frac{x}{H_1} < 7.0$. (c) FFT spectra on $\chi(t)$ and $Q(t)$ at $\frac{x}{H_1} = 1.5$.

analysis, taking into account a velocity profile where the slow and the speed profiles are linked through a continuous vorticity layer in the high-speed stream. This theoretical proposition, reported in Table 6, yields a value for the frequency f which differs from (12). It should however be kept in mind that this proposal is essentially a way to derive a scaling evolution, rather than a formula to accurately predict a frequency value, as explained in Ben Rayana (2007). The prefactor $\frac{1.5}{2\pi}$ in the formula presented in Table 6 remains indeed subject to controversy. While Raynal's (Raynal, 1997) experimental observations agree quite well with this prediction, Marmottant's results (Marmottant and Villermaux, 2004) differ with this prediction by a factor 3, and similarly so far for Ben Rayana's results (Ben Rayana, 2007). Finally, it should be noted that a coupling with the global flapping dynamics may also affect this primary interfacial instability frequency. In any case, a direct comparison with the theoretical prediction proposed in Table 6 is to be done with care.

This theoretical prediction involves the vorticity layer thickness δ_ω developing in the high-speed stream, computed as follows:

$$\delta_\omega = \frac{\Delta U}{max\left(\frac{dU}{dy}\right)} = \frac{U_2 - U_{interface}}{\frac{2U_2}{\delta_2}} = \frac{U_2 - U_{c_{Dimotakis}}}{\frac{2U_2}{\delta_2}}.$$

Raynal has shown that the interfacial velocity is well represented by the theoretical proposition of Dimotakis (1986) for a coherent structure developing in a single-phase shear-layer. This has been confirmed by Ben Rayana's experimental work, and more recently by the numerical works of Hoepffner et al. (2011) and Orazzo et al. (2011):

$$U_{c_{Dimotakis}} = \frac{\sqrt{\rho_1}U_1 + \sqrt{\rho_2}U_2}{\sqrt{\rho_1} + \sqrt{\rho_2}}.$$

Global oscillation frequency

Measurement method. The global oscillation frequency f_{flapp} of the flapping liquid sheet is measured by analyzing the signal recorded on a set probes similar to the ones described in section "Primary interfacial instability frequency" but regularly distributed in the x direction at $\frac{y}{H_1} = 0$ in the Oxy plane. The temporal evolution $\chi(t)$ at each measurement point is a superposition of Heaviside-like functions as illustrated in Fig. 10 for the location $\frac{x}{H_1} = 3.0$. Three such successive Heaviside functions define a whole flapping period: the first one corresponds to the liquid sheet crossing the axis $\frac{y}{H_1} = 0$ one way (say upward or for increasing value of y), the second one is produced when the sheet crosses $\frac{y}{H_1} = 0$ in the other way (downward or for decreasing value of y), and the third one is associated to the repetition of the upward motion through $\frac{y}{H_1} = 0$. The frequency obtained after FFT of $\chi(t)$ corresponds to twice the flapping frequency since two successive Heaviside functions define a half-period.

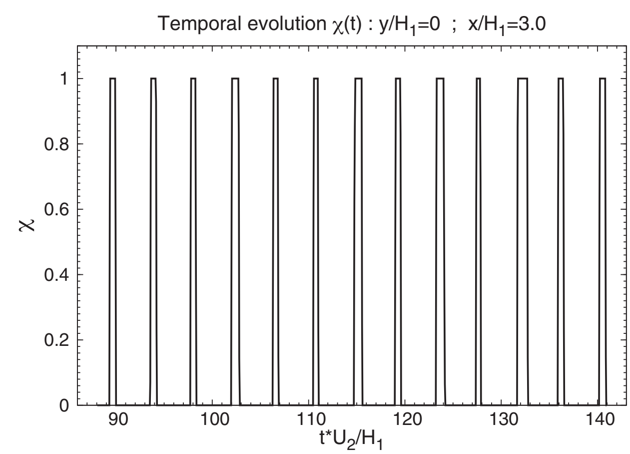

Fig. 10. Time evolution of $\chi(t)$ at point $(x^*, y^*, z^*) = (3, 0, 0)$.

Spectrogram analysis. Fig. 11 illustrates the spectrogram obtained at $\frac{y}{H_1} = 0$ for $\chi(x^*, 0, 0, t)$. This figure displays a low frequency which is

Table 7
Comparison of the flapping frequency computed in the present numerical experiment with existing propositions.

Authors	Proposed correlation	Result with author's proposition	Present study result
Carentz (2000)	$f_{flapp} = 0.1\sqrt{M}$	$f_{flapp} = 0.19\left(\frac{U_2}{H_1}\right)$	$f_{flapp} = 0.113\left(\frac{U_2}{H_1}\right)$
Fernandez et al. (2009)	$\frac{f_{flapp}H_1}{U_{min}} = \left(\frac{\rho_2(U_2-U_{min})c_{inj}}{\mu_l}\right)^{\frac{4}{5}}\left(\frac{\delta}{\delta_\omega}\right)^{\frac{3}{2}}$	Not computable[1]	
Carvalho et al. (2002)	$\frac{f_{flapp}H_1}{U_1} = 0.13M^{0.38}$	$\frac{f_{flapp}H_1}{U_1} = 0.211$	$\frac{f_{flapp}H_1}{U_1} = 0.68$
Larricq-Fourcade (2006)[2]	$\frac{f_{flapp}H_1}{U_1} = 0.0034\left(\frac{\rho_2(U_2-U_{min})^2}{\rho_1U_1^2}\right)^{\frac{1}{2}}\frac{\delta}{\delta_\omega}$	$\frac{f_{flapp}H_1}{U_1} = 0.0155$	$\frac{f_{flapp}H_1}{U_1} = 0.68$

[1] Proposition involves injector chord length c_{inj} specific to the experimental set-up.
[2] With $\delta_\omega = \frac{(U_2-U_1)}{\frac{2U_2}{\delta_2}}$.

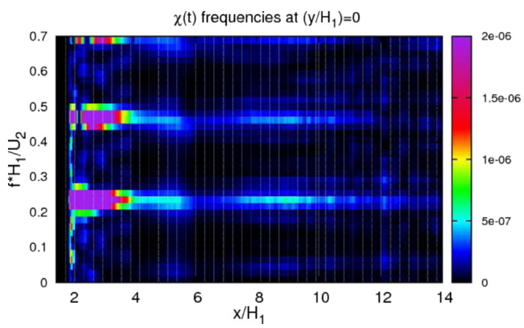

Fig. 11. Spectrogram performed at $\frac{y}{H_1} = 0$ on $\chi(x*, 0, 0, t)$, raising a constant frequency along downstream distance: $2 * f_{flapp} = 0.226\left(\frac{U_2}{H_1}\right)$.

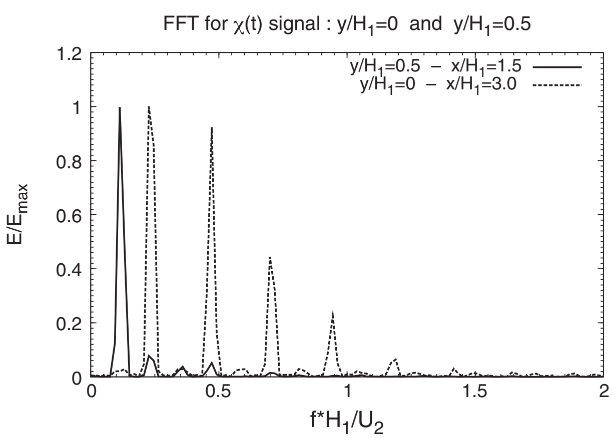

Fig. 12. Confrontation of primary interfacial instability frequency (full line) and double of the flapping instability frequency (dashed line).

the frequency of interest, followed by harmonics components, coming from the fact that the temporal signal is a crenel. The low frequency of Fig. 11 corresponds to twice the flapping frequency f_{flapp}, that is:

$$2 * f_{flapp} = 0.226\left(\frac{U_2}{H_1}\right) \tag{13}$$

The flapping frequency is found constant with downstream distance, in agreement with previous studies (Mansour and Chigier, 1991; Carvalho et al., 2002; Zuzio et al., 2013).

The primary interfacial instability is found equal to the flapping frequency, as illustrated in Fig. 12, showing that those two phenomena are strongly linked. To the author's knowledge, no primary instability frequency has been previously measured on a flapping liquid sheet. If a strong link is noticeable in the present simulations, it is however hard to decide which instability is imposing its frequency on the other.

Table 8
Estimate of the flapping frequency for the present numerical experiment using some available propositions of Strouhal number formulae.

Authors	Proposed Strouhal number	Strouhal number obtained using frequency of present study
Lozano and Barreras (2001b)[1]	$\frac{f_{flapp}H_1}{U_2-U_{min}} \simeq 0,01$	$\frac{f_{flapp}H_1}{U_2} = 0.11$
Lozano et al. (2005)[2]	$0.01 < \frac{f_{flapp}\sqrt{H_2H_1}}{U_2-U_{min}} < 0,015$	$\frac{f_{flapp}\sqrt{H_2H_1}}{U_2} = 0.26$
Couderc (2007)	$\frac{fH_1\sqrt{\delta_2}}{2U_2\sqrt{H_2}} \simeq 0.02$	$\frac{fH_1\sqrt{\delta_2}}{2U_2\sqrt{H_2}} = 0.007$

[1] Hypothesis: $U_{min} = 0$.
[2] Hypothesis: $\frac{H_2}{H_1} = 5.5$.

Comparison with existing propositions. The computed flapping frequency is compared with existing propositions of evolution law for the flapping frequency or the Strouhal number, summarized in Tables 7 and 8. When the proposition involves the height H_2 as characteristic length, an adjustment to the periodic setting of the present calculation is needed: the value H_2 is taken equal to $H_2 = 5.5H_1$ (see Fig. 1).

The scattering of the results shows how hard it is to derive a universal proposition describing the evolution of the flapping frequency with the flow parameters. This difficulty results from the large number of parameters involved in the flow dynamics, among which the geometry, the boundary layer thicknesses, the velocities and their ratio, the densities and their ratio, the momentum flux ratio. To establish the correlations presented in Tables 7 and 8, authors have studied several geometries and a wide range of velocities, but except for the correlation proposed in Fernandez et al. (2009) ($r_\rho = 1000$ to 100) and the one proposed in Couderc (2007) ($r_\rho = 80$), all the other propositions are established with water (or kerosene) and air at atmospheric pressure, leading to a density ratio of about $r_\rho = 1000$.

As discussed in the introduction, the choice of a moderate density ratio retained in this work ($r_\rho = 10$), allows to perform for a limited computational cost the flapping liquid sheet configurations analyzed in section "Flow configurations and numerical parameters" (evolution of the flapping frequency with the high-speed stream velocity U_2), section "Flapping dynamics: mechanism and characterization" (flapping dynamics for the physical parameters defined in Table 1) and section "Influence of the high-speed stream initial boundary layer thickness" (influence of the high-speed stream initial boundary layer thickness). Since the density ratio, along with the momentum flux ratio and the velocity ratio, is included in some of the correlations of Table 3, a limited range of validity for these correlations as far as the density ratio is concerned might be a possible explanation for the scattering of values observed in Tables 7 and 8. Also note that this scattering is also present for correlations established with the same range of (high) density ratios in the experiments but a different range for the velocity ratio and/or the momentum flux ratio; this can be interpreted once again as the sign the validity of the proposed

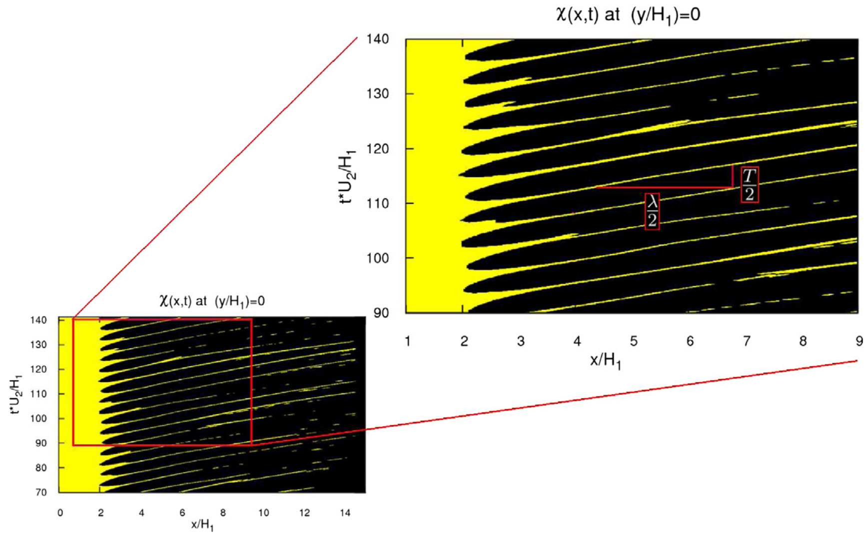

Fig. 13. Flapping wavelength λ and period T, on spatio-temporal diagram of binary function $\chi(x, t)$ at $\frac{y}{H_1} = 0$.

correlations is actually limited to a specific range of values for the non-dimensional numbers used to build them.

Convective speeds

The flapping liquid sheet is convected downstream. As the flapping motion is said to be responsible to the break-up phenomenon (see Carentz, 2000), it is of interest to evaluate its convective speed, for a prediction of the droplets' velocity.

Flapping convective speed

The convective speed of the flapping sheet is assessed from the spatiotemporal diagram presented in Fig. 13, also called Hovmöller diagram and which displays the spatiotemporal evolution of $\chi(x, t)$ at $\frac{y}{H_1} = 0$. More precisely, Fig. 13 displays the region where $\chi(x, 0, 0, t) = 1$ in yellow (presence of liquid) and where $\chi(x, 0, 0, t) = 0$ in black (presence of the high-speed stream). For a fixed position, the Heaviside-like temporal evolution of $\chi(x, 0, 0, t)$ described in section "Global oscillation frequency" is clearly evidenced in Fig. 13. Half of the flapping period is reported on this figure, as well as half of the flapping wavelength. The distinctive slope which can be identified on this diagram is equal to the inverse of the flapping sheet's convective speed. The slope measurement is performed for $3.5 < \frac{x}{H_1} < 8.0$ and the evaluated convective speed is:

$$\frac{U_{c_{flapp}}}{U_2} = 0.64 \tag{14}$$

Lozano and Barreras (2001b) found in his physical experiment that the convective speed of the liquid sheet is varying along the downstream distance. Such a variation is not observed in the present numerical experiment. A possible explanation is the lack of gravity in the present simulations, that would be directed in parallel to the flow with a streamwise orientation and that could induce a liquid acceleration.

When spatiotemporal diagrams performed on $\chi(x, 0, 0, t) = 1$ and on positives values of Q criterion $Q(x, 0, 0, t)$, identifying coherent structures, are superimposed (see Fig. 14), it can be observed the slopes of both diagrams match perfectly well. The meaning of this observation is that the advection of the liquid sheet and the of the vortical structures, initially induced by vortical detachment behind the primary interfacial instability, are synchronous physical phenomena.

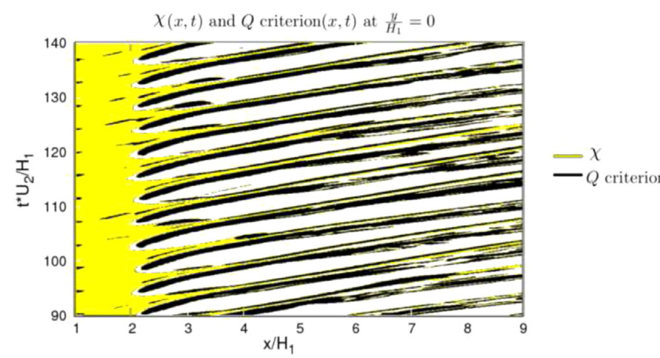

Fig. 14. Superposition of spatio-temporal diagram for indicating phase function $\chi(x, t)$ (in yellow) positive values of Q criterion $Q(x, t)$ (in black) at $\frac{y}{H_1} = 0$. (For interpretation of the references to color in this figure legend, the reader is referred to the web version of this article.)

Primary interfacial instability convective speed

After having characterized the convective speed of the whole liquid sheet, we focus in this part on the primary instability's convective speed. This study is thus performed at $\frac{y}{H_1} = 0.5$, the interface initial position in the upper part of the domain. The corresponding frequential analysis has been presented in section "Primary interfacial instability frequency". The spatiotemporal diagram in Fig. 15 displays the evolution of the indicating phase function $\chi(x, t)$ at $\frac{y}{H_1} = 0.5$. A change in the slope can be clearly observed for positions $2.0 < \frac{x}{H_1} < 3.5$; this slope modification can be interpreted as a change in convective speed, which occurs between the liquid core characterized by L_{core} and the flapping distance L_{flapp}.

- The measured slopes for positions $\frac{x}{H_1} \le 2.0$ yield a first convective speed $U_{c_{1st}}$, for $\frac{x}{H_1} \le L_{core}$:

$$\frac{U_{c_{1st}}}{U_2} = 0.33 \tag{15}$$

Note that this convective speed is in good agreement with the theoretical prediction proposed in Dimotakis (1986) for a coherent structure in a single-phase shear-layer, and confirmed by several authors (Raynal, 1997; Ben Rayana, 2007; Hoepffner et al., 2011; Orazzo et al., 2011) to be the convective speed of a

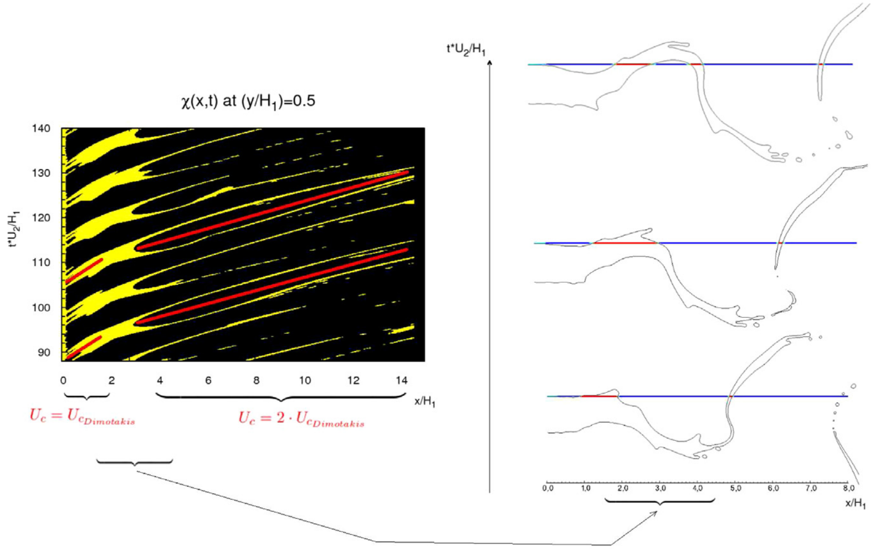

Fig. 15. Spatiotemporal diagram for the indicating phase function computed at $\frac{y}{H_1} = 0.5$.

Kelvin–Helmholtz interfacial wave for a sheared interface:

$$\frac{U_{c_{Dimotakis}}}{U_2} = \frac{\left(\frac{\sqrt{\rho_2}U_2+\sqrt{\rho_1}U_1}{\sqrt{\rho_2}+\sqrt{\rho_1}}\right)}{U_2} = 0.36 \tag{16}$$

- The measured slopes for positions $\frac{x}{H_1} \geq 3.5$ yield the convective speed $U_{c_{flapp}}$, for $\frac{x}{H_1} \geq L_{flapp}$:

$$\frac{U_{c_{flapp}}}{U_2} = 0.65 \tag{17}$$

This convective speed $U_{c_{flapp}}$, which is the convective speed of the whole flapping sheet, is found to be about twice of $U_{c_{1st}}$, the primary instability convective speed.

Influence of the high-speed stream initial boundary layer thickness

The analysis performed in the previous section corresponds to the fixed set of physical parameters summarized in Table 1. It was pointed out in the introduction of this work the high-speed stream boundary layer thickness δ_2 is suspected to influence the flapping dynamics in a crucial way but it was also emphasized this parameter remains hard to measure hence to control experimentally. Consequently, since the choice of a low density ratio between the liquid jet and the surrounding fast stream allows for a sensitivity study by keeping the computational cost of each flow configuration moderate, the flow parameter δ_2 is varied in this section, with all the other physical parameters of Table 1 kept constant. Successive simulations are performed with

$$\frac{\delta_2}{H_1} = 0.1;\ 0.3;\ 0.5;\ 0.7;\ 1.0;\ 1.2$$

on top of the previous calculation corresponding to the choice $\frac{\delta_2}{H_1} = 0.1$ and the sensitivity of the average quantities and flapping characteristics (flapping frequency and wavelength, convective speeds, spatial amplification growth rate) to δ_2 are carefully analyzed.

Influence of δ_2 on the global flow picture

Fig. 16 provides an overview of the typical flow dynamics for $\delta_2 = 1.0\,H_1$, to be compared with the previous global flow picture 4 obtained for $\delta_2 = 0.1\,H_1$. When strongly increasing δ_2, the flapping

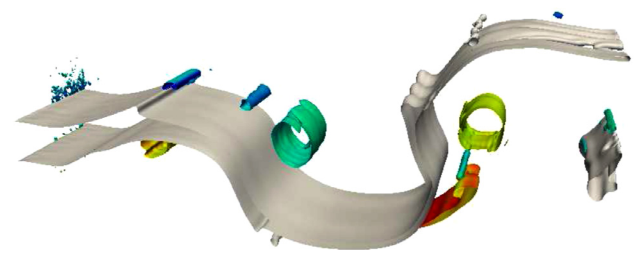

Fig. 16. Instantaneous contours of interface (in grey) and of Q criterion $Q = 0.3(\frac{U_2}{H_1})^2$ colored by spanwise vorticity, for $\delta_2 = 1.0$.

dynamic is preserved, as well as the development process of an interfacial wave and the vortical recirculation in the high-speed stream behind this wave. The vortical structures are now two-dimensional, and the sheet is no longer subject to break-up. Compared to the case where $\frac{\delta_2}{H_1} = 0.1$, the liquid core seems to be more extended and the spatial amplification growth rate seems to be smaller. The analysis of the flow dynamics also suggests that the flapping frequency has decreased (see Section "Influence on the flapping frequency").

Influence of δ_2 on average quantities

The average liquid profiles and velocity profiles of each phases at $\frac{x}{H} = 3.0$ computed for the six increasing values of δ_2/H_1 between 0.1 and 1.2 are presented in Fig. 17. The increase of δ_2 induces a decrease in the shear imposed by the high-speed stream to the liquid: $\mu_2(\frac{\partial U_2}{\partial y})_0 \simeq \mu_2\frac{U_2}{\delta_2}$. The velocity profiles of the liquid $\langle U\rangle_1$ (see 17(b)) display a less and less pronounced liquid acceleration as δ_2 is increased. The sheet thinning, for flowrate conservation reason, evolves therefore in the same way. With increasing δ_2, the sheet becomes larger, locally more massive, and is therefore harder to destabilize. The average liquid rate $\alpha(x)$ illustrates the liquid core increase with the increase of δ_2 (see 17(a)). The velocity profiles of the high-speed stream $\langle U\rangle_2$ (see 17(c)) show that the merging process of the high-speed stream and liquid velocity profiles is less and less pronounced with the increase of δ_2.

The evolution with δ_2 of average quantities along the horizontal line $\frac{y}{H_1} = 0$ are presented in Fig. 18. The liquid core lengthening and the increase of the downstream distance needed for the liquid acceleration with the increase of δ_2 are clearly illustrated.

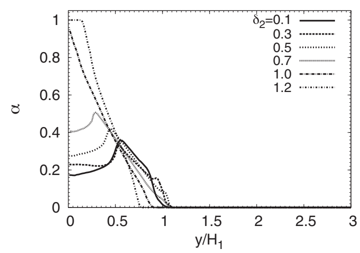

(a) Increase of the liquid core with δ_2 and shortening of the area reached by the liquid.

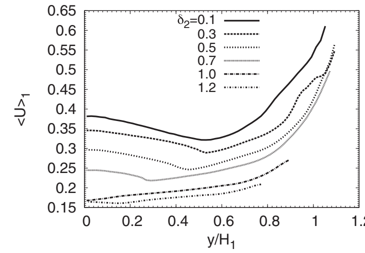

(b) Less and less pronounced liquid acceleration with the increase of δ_2.

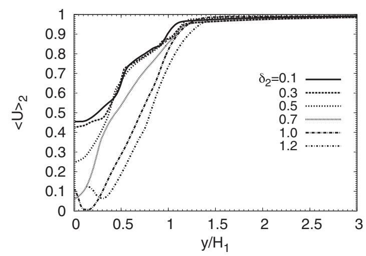

(c) Reduction of liquid entrainment capacity with increasing δ_2.

Fig. 17. Evolution with δ_2 of average quantities at $\frac{x}{H_1} = 3.0$.

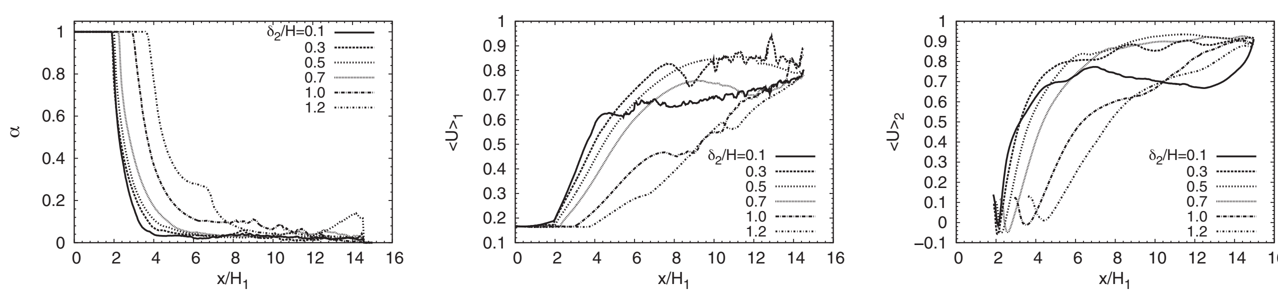

Fig. 18. Evolution with δ_2 of average quantities along $\frac{y}{H_1} = 0$.

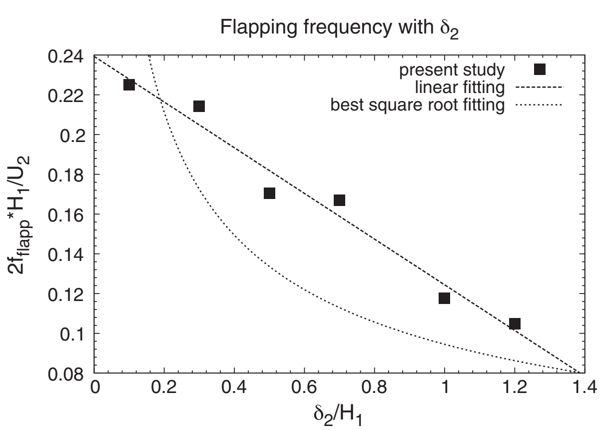

Fig. 19. Evolution of the flapping frequency with δ_2. Best fiting with a linear function and with Couderc's (2007) proposition.

Influence of δ_2 on flapping characteristics

Influence on the flapping frequency

The flapping frequeny is found to evolve linearly with δ_2, as shown in Fig. 19. Note this result is not in agreement with Couderc's numerical study (Couderc, 2007) where, for the same range of $\frac{\delta_2}{H_1}$, an evolution of the flapping frequency proportional to $\frac{1}{\sqrt{\delta_2}}$ was found. A possible explanation for this discrepancy is that Couderc's results were based on two-dimensional computations. It is well known the size of the vortical structures in the high-speed stream are overestimated for such 2D calculations, which is likely to result in global dynamics distinct from the one observed in the more physically relevant 3D case. Another possible explanation lies in the fact that the physical parameters (velocities, densities, viscosities) used in the present numerical experiments differ from the one used by Couderc, and this could lead to another flow regime.

Influence on flapping wavelength

The wavelength evolution with δ_2 is presented in Fig. 20. The wavelength measurement is based on Hovmöller diagrams, such as the one presented in Fig. 13. For each time and for every positions the distance between two locations of $\chi(x, 0, 0, t) = 1$ is calculated. The wavelength measurement is rather inaccurate because this distance is varying, especially when considering positions between $2 < \frac{x}{H_1} < 4$ (see Fig. 13). Moreover, the breakup phenomenon increases the inaccuracy of the wavelength measurement. The final value retained is the average of all the computed wavelengths. In spite of these difficulties and uncertainties, a wavelength increase with the increase of δ_2

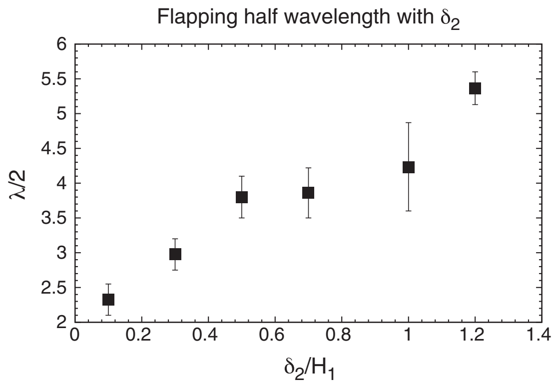

Fig. 20. Evolution of the flapping wavelength with δ_2.

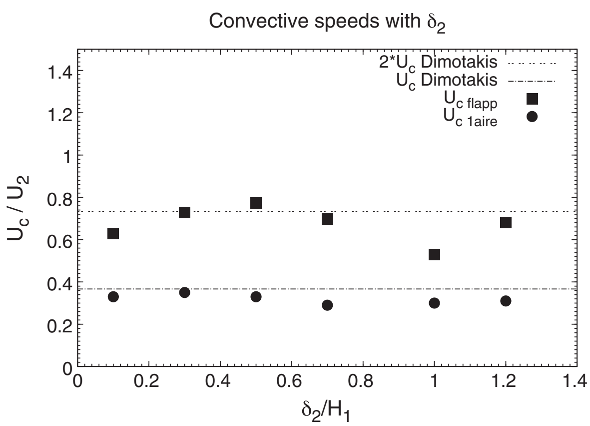

Fig. 21. Evolution of the convective speed with δ_2.

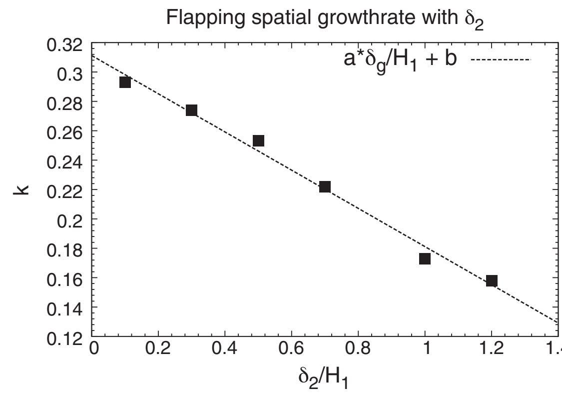

Fig. 22. Evolution of the growth factor with δ_2.

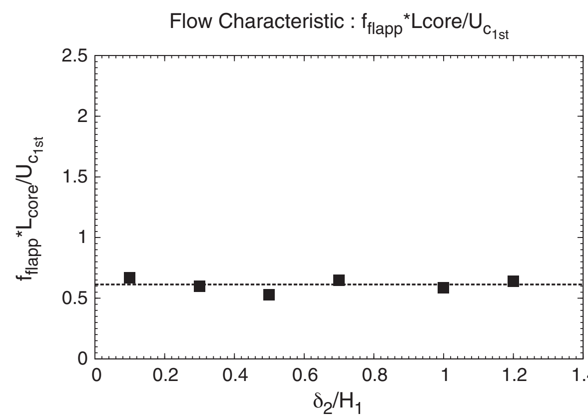

Fig. 23. Insensitivity of the quantity $\frac{f_{flapp}*L_{core}}{U_{c_1st}}$ to the modification of δ_2. The quantity $\frac{f_{flapp}*L_{core}}{U_{c_1st}}$ remains constant and equal to 0.613.

can nonetheless be observed in Fig. 20, following an approximatively linear law.

Influence on convective speeds

A linear variation of both the frequency and the wavelength suggests the convective speed of the flapping sheet remains constant when δ_2 varies. The evolution of the convective speeds with δ_2 is presented in Fig. 21. The primary interfacial instability has a convective speed approximatively equal to the theoretical prediction of Dimotakis (1986), and the whole flapping sheet has a convective speed approximatively equal to twice this theoretical prediction, whatever the value of δ_2/H_1 in the range [0.1, 1.2].

Influence on spatial amplification growth rate

The evolution of the spatial amplification growth rate with the increase of δ_2 is presented in Fig. 22. A linear decrease of k with respect to δ_2 can be observed.

Characteristic quantity of the flapping dynamics

When modifying δ_2, a constant decrease in the frequency has been observed, as well as an increase of the liquid core. Fig. 23 displays the quantity $\frac{f_{flapp}L_{core}}{U_{c_{1st}}}$ as a function of δ_2. It is found the proposed Strouhal-like number remains constant with the modification of δ_2. For the computations performed, this constant is equal to 0.613. The way the proposed Strouhal number is built underlines the importance of the liquid core resulting from the flapping dynamics. The L_{core} quantity could be the effective characteristic length to take into account for building a Strouhal number, rather than the liquid sheet thickness H_1 as proposed by several authors (see Tables 7 and 8). It would be interesting to assess whether this liquid core length proves to be relevant for building a Strouhal number in experimental flapping jets.

Conclusions

The flapping mechanism of a liquid sheet sheared on both sides by a high-speed stream has been numerically studied using direct numerical simulation. The YALES2 solver has been used to perform a series of numerical experiments on a flapping liquid sheet sheared by a high-speed stream. The liquid-to-gas density ratio considered in these numerical experiments was rather low with respect to typical physical experiments but allowed to perform a sensitivity study of the flow features to some key physical parameters thanks to a reasonable computational cost. It was observed that a primary interfacial instability is developing on both interfaces of the liquid sheet, leading itself to the development of an interfacial wave. Behind this interfacial wave a vortical detachment occurs in the high-speed stream, which modifies the pressure field around the liquid sheet. The flapping behavior is eventually a consequence of the pressure difference on both sides of the liquid sheet. The flapping sheet was quantitatively analyzed through average quantities such as liquid core length, flapping length and spatial amplification growth rate. Frequencies of interest were also identified: primary interfacial instability frequency and global oscillation frequency. The equality between both frequencies suggests a strong link between the primary interfacial instability and the global flapping phenomenon. Convective speeds were also computed from the analysis of spatiotemporal diagrams. The set of data drawn from this in-depth analysis is a reference of interest for future propositions of normalized laws describing the flapping dynamics.

A sensitivity study to the initial high-speed stream boundary layer thickness δ_2 has been performed in order to assess the impact of this physical parameter on the flapping characteristics. The flapping frequency is found to decrease linearly with the increase of δ_2 while the flapping wavelength increases approximatively linearly with the increase of δ_2. The convective speeds of the primary interfacial instability and of the whole flapping sheet are found to be constant with the modification of δ_2. The convective speed of the primary interfacial instability is approximatively equal to the theoretical prediction done in Dimotakis (1986), and the whole flapping sheet has a convective speed about twice that of the primary interfacial instability. Finally, it was proposed to define a Strouhal number for the flapping sheet using the flapping frequency, the liquid core length and the convective speed of the primary interfacial instability, namely $\frac{f_{flapp} L_{core}}{U_{c_1 st}}$. It was concluded from the sensitivity study this Strouhal number remains constant with the modification of δ_2. This suggests the liquid core induced by flapping dynamics would be a relevant characteristic length of the flapping dynamics. It would be of interest to check whether this length and the proposed Strouhal number remain characteristic for other flapping configurations, in particular for coaxial configurations. Future work will thus be devoted to a better understanding, through direct numerical simulation, of the flapping behavior in coaxial case and how the flapping dynamics influences the atomization process.

Acknowledgments

This work has been supported by the Carnot Institute “Energies du Futur”. The laboratory LEGI is part of the LabEx Tec 21 (Investissements dAvenir - grant agreement nANR-11-LABX-0030). Part of computing resources were provided by IDRIS-CNRS and CIMENT infrastructure (GRANT CPER07_13 CIRA). We also acknowledge PRACE for awarding CPU time on the Curie machine based in France at TGCC (CEA) under the grant 2012061113.

References

Ben Rayana, F., 2007. Contribution à l’étude des instabilités interfaciales liquide-gaz en atomisation assisté et tailles des gouttes. Ph.D. thesis. Institut National Polytechnique de Grenoble.

Berlemont, A., Bouali, Z., Cousin, J., 2012. Simulation of liquid/gas interface break-up with a coupled Level Set/VOF/Ghost Fluid method. Proceedings of the Seventh International Conference on Computational Fluid Dynamics.

Carentz, H., 2000. Etude de la pulvérisation d’une nappe liquide mince. Ph.D. thesis. Université Pierre et Marie Curie.

Carvalho, I.S., Heitor, M., Santos, D., 2002. Liquid film desintegration regimes and proposed correlations. Int. J. Multiph. Flow 28, 773–789.

Couderc, F., 2007. Développement d’un code de calcul pour la simulation d’écoulements de fluides non miscibles. Application à la désintégration assistée d’un jet liquide par un courant gazeux. Ph.D. thesis. ENSAE Toulouse.

Desjardins, O., Mccaslin, J.O., Owkes, M., Brady, P., 2013. Direct numerical and large-eddy simulation of primary atomization in complex geometries. At. Sprays 23, 1001–1048.

Desjardins, O., Moureau, V., 2010. Methods for multiphase flows with high density ratio. In: Proceedings of the Center for Turbulent Research, Summer Program 2010, pp. 313–322.

Desjardins, O., Moureau, V., Pitsch, H., 2008. An accurate conservative level set/ghost fluid method for simulating turbulent atomization. J. Comput. Phys. 227, 8395–8416. doi:10.1016/j.jcp.2008.05.027.

Dimotakis, P.E., 1986. Two-dimensional shear-layer entrainment. AIAA J. 24, 1791–1796.

Engelbert, C., Hardalupas, Y., Whitelaw, J.H., 1995. Breakup phenomena in coaxial airblast atomizers. Proc. Roy. Soc. A: Math. Phys. Eng. Sci. 451, 189–229. doi:10.1098/rspa.1995.0123.

Enjalbert, N., 2006. Modélisation avancée de la combustion turbulente diphasique en régime de forte dilution par les gaz brûlés. Ph.D. thesis. Institut National Supérieur des Sciences Appliquées de Rouen.

Eroglu, H., Chigier, N., Farago, Z., 1991. Coaxial atomizer liquid intact lenghts. Phys. Fluids A 3, 303–308.

Fernandez, V.G., Berthoumie, P., Lavergne, G., 2009. Liquid sheet desintegration at high pressure: an experimental approach. C.R. Mecanique 337, 481–491.

Fuster, D., Bagué, A., Boeck, T., Le Moyne, L., Leboissetier, A., Popinet, S., Ray, P., Scardovelli, R., Zaleski, S., 2009. Simulation of primary atomization with an octree adaptive mesh refinement and VOF method. Int. J. Multiph. Flow 35, 550–565. doi:10.1016/j.ijmultiphaseflow.2009.02.014.

Fuster, D., Matas, J.-P., Marty, S., Popinet, S., Hoepffner, J., Cartellier, A., Zaleski, S., 2013. Instability regimes in the primary breakup region of planar coflowing sheets. J. Fluid Mech. 736, 150–176. doi:10.1017/jfm.2013.536.

Grout, S., Dumouchel, C., Cousin, J., Nuglisch, H., 2007. Fractal analysis of atomizing liquid flows. Int. J. Multiph. Flow 33, 1023–1044.

Herrmann, M., 2008. A balanced force refined level set grid method for two-phase flows on unstructured flow solver grids. J. Comput. Phys. 227, 2674–2706. doi:10.1016/j.jcp.2007.11.002.

Herrmann, M., 2010. A parallel Eulerian interface tracking/Lagrangian point particle multi-scale coupling procedure. J. Comput. Phys. 229, 745–759. doi:10.1016/j.jcp.2009.10.009.

Hoepffner, J., Blumenthal, R., Zaleski, S., 2011. Self- similar wave produced by local perturbation of the Kelvin–Helmholtz shear-layer instability. Phys. Rev. Lett. 106, 104502.

Hunt, J.C.R., Wray, A.A., Moin, P., 1988. Proceedings of the 1988 Summer Program. CTR Standford.

Kim, B.D., Moin, P., 2011. Numerical simulation of the breakup of a round liquid jet by a coaxial flow of gas with a subgrid Lagrangian breakup model. Center Turbul. Res., Annu. Res. Briefs.

Larricq-Fourcade, C., 2006. Etude de la pulvérisation assistée en air d’une nappe liquide et influence d’un vent ionique sur les instabilités hydrodynamiques. Ph.D. thesis. ENSAE Toulouse.

Lasheras, J.C., Villermaux, E., Hopfinger, E.J., 1998. Break-up and atomization of a round water jet by a high-speed annular air jet. J. Fluid Mech. 357, 351–379. doi:10.1017/S0022112097008070.

Leboucher, N., Roger, F., Carreau, J., Claverie, A., 2009. Atomization process of an annular liquid sheet assisted by an inner gas jet. In: Proceedings of the 11th Triennial International Annual Conference on Liquid Atomization and Sprays Systems (ICLASS). Vail, Colorado.

Leroux, B., Delabroy, O., Lacas, F., 2000. Experimental study of coaxial atomizers scaling. PartI: dense core zone. At. Sprays. 17, 381–407.

Lozano, A., Barreras, F., 2001. Experimental study of the gas flow in an air-blasted liquid sheet. Exp. Fluids 31, 367–376. doi:10.1007/s003480100301.

Lozano, A., Barreras, F., 2001. Longitudinal instabilities in an air-blasted liquid sheet. J. Fluid Mech. 437, 143–173.

Lozano, A., Barreras, F., Siegler, C., Löw, D., 2005. The effects of sheet thickness on the oscillation of an air-blasted liquid sheet. Exp. Fluids 39, 127–139. doi:10.1007/s00348-005-0989-1.

Malandain, M., 2013. Simulation massivement parallèle des écoulements turbulents à faible nombre de Mach. Ph.D. thesis. Institut National Supérieur des Sciences Appliquées de Rouen.

Malandain, M., Maheu, N., Moureau, V., 2013. Optimization of the deflated Conjugate Gradient algorithm for the solving of elliptic equations on massively parallel machines. J. Comput. Phys. 238, 32–47. doi:10.1016/j.jcp.2012.11.046.

Mansour, A., Chigier, N., 1991. Dynamic behavior of liquid sheets. Phys. Fluids 12, 2971–2980.

Marmottant, P., 2001. Atomisation d’un liquide par un courant gazeux. Ph.D. thesis. Institut National Polytechnique de Grenoble.

Marmottant, P., Villermaux, E., 2004. On spray formation. J. Fluid Mech. 498, 73–111. doi:10.1017/S0022112003006529.

Matas, J.-P., Cartelier, A., 2013. Flapping instability of a liquid jet. C.R. Acad. Sci. - Ser. IIB - Mech. 341, 35–43.

Matas, J.-P., Marty, S., Cartellier, A., 2011. Experimental and analytical study of the shear instability of a gas-liquid mixing layer. Phys. Fluids 23, 094112. doi:10.1063/1.3642640.

Menard, T., Tanguy, S., Berlemont, A., 2007. Coupling level set/VOF/ghost fluid methods: validation and application to 3D simulation of the primary break-up of a liquid jet. Int. J. Multiph. Flow 33, 510–524. doi:10.1016/j.ijmultiphaseflow.2006.11.001.

Orazzo, A., Coppola, G., De Luca, L., 2011. Single-wave Kelvin-Helmholtz instability in nonparallel channel flow. At. Sprays 21, 775–785.

Park, J., Kang, H., Xianguo, L., Metin, R., 2004. Experimental investigation on cellular breakup of a planar liquid sheet from an air-blast nozzle. Phys. Fluids 16, 625–632.

Porcheron, E., Carreau, J.-L., Prevost, L., LeVisage, D., Roger, F., 2002. Effects of density on coaxial liquid jet atomization. At. Sprays 12, 209–227.

Raynal, L., 1997. Instabilité et entraînement à l’interface d’une couche de mélanche liquide-gaz. Ph.D. thesis. Institut National Polytechnique de Grenoble.

Shinjo, J., Umemura, A., 2010. Simulation of liquid jet primary breakup: dynamics of ligament and droplet formation. Int. J. Multiph. Flow 36, 513–532. doi:10.1016/j.ijmultiphaseflow.2010.03.008.

Shinjo, J., Umemura, A., 2011. Surface instability and primary atomization characteristics of straight liquid jet sprays. Int. J. Multiph. Flow 37, 1294–1304. doi:10.1016/j.ijmultiphaseflow.2011.08.002.

Stapper, B., Samuelsen, G.S., 1990. An experimental study of the breakup of a two-dimensional liquid sheet in the presence of co-flow air shear. AIAA Pap. 89–0461.

Vantieghem, S., 2011. Numerical Simulation of Quasi-static Magnetohydrodynamics using an Unstructured Finite Solver: Development and Applications. Ph.D. thesis. Université Libre de Bruxelles.

Woodwart, R.D., 1993. Primary Atomization of Liquid Jets Issuing from Rocket Engine Coaxial Injectors. Ph.D. thesis. Department of Mechanical Engineering, The Pennsylvania State University, University Park, PA.

Zuzio, D., Estivalezes, J.-L., Villedieu, P., Blanchard, G., 2013. Numerical simulation of primary and secondary atomization. C.R. Mécanique 341, 15–25. doi:10.1016/j.crme.2012.10.003.